ADVANCED FUNCTIONAL MATERIALS
www.afm-journal.de

Ultrahigh Infrared Photoresponse from Core–Shell Single-Domain-VO_2/V_2O_5 Heterostructure in Nanobeam

Zejun Li, Zhenpeng Hu, Jing Peng, Changzheng Wu, Yuchen Yang, Feng Feng, Peng Gao, Jinlong Yang, and Yi Xie**

Infrared (IR) harvesting and detection in red and near-IR (NIR) part of the solar spectrum have always been a long-term research area of intense interest. However, limited choices of current photoactive materials have significantly hampered the realization of ultrahigh IR sensitivity under room temperature conditions. The trigger for this requires the exploration of new photoactive materials and the ability to fabricate new photoactive structural design. Herein, a new oxide-catalogue photoconductive NIR detector with ultrahigh performance built by core/shell nanobeam heterostructures (CSNHs) with the inner single-domain monoclinic VO_2 (M) core and outer V_2O_5 shell, which is the first example of photoconductive IR detector made from transition metal oxides (TMOs), is presented. Benefited from the well-defined TMO heterojunction interface, the ultrahigh responsivity (R_λ) of 2873.7 A W^{-1} and specific detectivity (D*) of 9.23×10^{12} Jones are achieved at room temperature (at 990 nm; 0.2 mW cm^{-2}), recording the best performance compared with those reported IR detectors based on heavy-metal-free materials, and even comparable/superior to those traditional ones made from materials including heavy metals. These findings pave a new way to design oxide heterostructures for intriguing applications in optoelectronic and energy harvesting nanodevices.

1. Introduction

IR light harvesting and detection have attracted extensive interest bringing the intriguing applications of photovoltaic solar cells,[1] IR imaging,[2] and smart response devices.[3] IR detector is a detector that finely reacts to IR radiation, mainly including two types: thermal and photoconductive detectors. The thermal IR detectors relied on temperature dependent response, with slow response, low sensitivity but higher working temperature.[4] For the photoconductive IR detectors, the electrical signal of the detector is monitored by electronic excitations caused by the IR photons, resulting in faster response, higher sensitivity but cryogenic working temperature for reducing thermal noise.[5] In order to better keep tracking photons for photoconductive IR detectors, photoactive materials assuming a narrow bandgap are essential which would be sure to convert IR photons into electric signals with high quantum efficiency. For narrow band-gap semiconductors (NBSs), either traditional heavy-metal-including materials like HgCdTe[6] (<0.1 eV), HgTe[7] (0–0.68 eV), or PbS quantum dots[8] (QDs) (0.4–2 eV), and so on, or heavy-metal-free materials such as MoS_2[9] (1.2 eV), In_2Te_3[10] (1.19 eV), semiconducting single-wall carbon nanotubes (s-SWCNTs),[11] or semiconducting graphene nanoribbons[12] et al. The hybrid structures of QDs with the conducting materials, such as SWCNT/QDs and graphene/QDs composites, further improved the capability of IR photons harvesting and detection owing to the efficient charge separation and faster carrier mobility.[13] In the other aspect, artificially-designed sub-energy-level materials with smaller energy gap, which allow effective generation of IR photogenerated carriers, also attracted great attention. For example, quantum cascade IR detector,[14] GaAs based quantum well IR detectors (QWIDs).[15] However, current fabrication of ultrahigh performance photoconductive IR detectors is significantly limited by the choices of photoactive materials; nowdays, such challenges still present concerning with achieving high sensitivity and well stability at a high working temperature, as well as disposing environmental problems which come from the heavy-metal-including elements.

Photoconductive IR detectors based on transition metal oxides (TMOs) have been a trigger for IR harvesting and detection for advantages as follows: easy to achieve, "green" as well as excellent stability of TMOs systems. However, TMO materials still remain an unexplored field for photoconductive IR detectors with high IR response so far. Among the TMOs family, vanadium oxides offer a promising platform for photoconductive

Dr. Z. J. Li, Mr. J. Peng, Prof. C. Z. Wu, Dr. F. Feng, Prof. J. L. Yang, Prof. Y. Xie
Hefei National Laboratory for Physical Sciences at the Microscale
University of Science and Technology of China
Hefei, Anhui, 230026, P. R. China
E-mail: czwu@ustc.edu.cn; yxie@ustc.edu.cn
Prof. Z. P. Hu
School of Physics
Nankai University
Tianjin, 300071, P. R. China
Dr. Y. C. Yang
Department of Physics and Astronomy
University of Utah
Salt Lake City, Utah, 84112, USA
Prof. P. Gao
Department of Modern Mechanics
University of Science and Technology of China
Hefei, Anhui, 230026, P. R. China

DOI: 10.1002/adfm.201302967

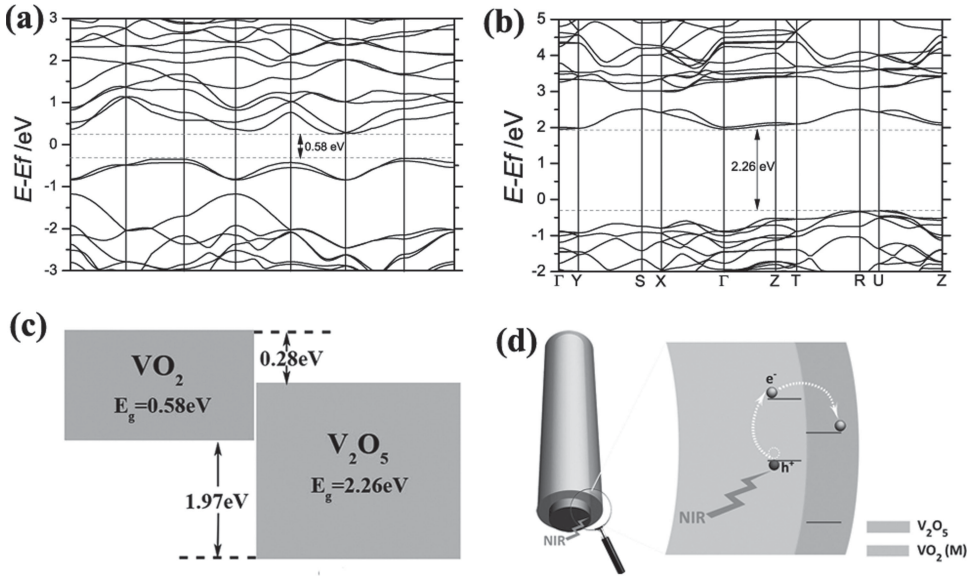

Figure 1. Theoretical analyses of VO_2 (M)/V_2O_5 heterostructure interface. a–b) Band structure of monoclinic VO_2 (M) (a) and orthorhombic V_2O_5 (b) calculated by the density functional calculations. c) Schematic diagram exhibiting the energy band structure of the VO_2 (M)/V_2O_5 heterostructures. The energy level of the O_{2s} was taken as zero reference in the calculations of the band alignment. d) The schematic illustration of the monoclinic VO_2 (M)/V_2O_5 core/shell nanobeam heterostructures, and the photogenerated carriers transfer in the heterointerface under NIR illumination.

IR detector with high rate and efficiency of detection due to both the fine regulation of their band structure coming from numerous valence states and rich coordination-style configurations.[16] Especially, monoclinic VO_2 (M) nanobeam has unique advantages to be the optimal candidate for IR detection. First of all, its narrow bandgap (only 0.58 eV) will optimize the efficiency. Secondly, the one dimensional single-domain VO_2 (M) nanobeam structure with high surface-to-volume ratio will inevitably lead to significant purification of the electrical behavior which is significantly sensitive to environmental perturbation. The synergic advantages of small band gap and single phase domain in monoclinic VO_2 (M) nanobeam serve an ideal platform to achieve a high response upon external IR photons stimulus. Nonetheless, pure VO_2 (M) nanobeam is still disadvantaged from easy recombination of the photogenerated excitons (electron-hole pairs) due to its relatively low dielectricity. Regarding this, the issue of efficient dissociation of excitons becomes a crucial step. One solution to this problem is to construct heterointerface[17] in order to generate a built-in electric field. Structural analysis and theoretical calculations have confirmed that VO_2 (M)-V_2O_5 heterointerface forms a type ‖ heterojunction as shown in **Figure 1**c. The staggered band alignment between inner monoclinic VO_2 nanobeam core and outer V_2O_5 shell as depicted in Figure 1d would efficiently prolong the lifetime of excitons so as to improve the IR harvesting and detection performance. Therefore, monoclinic VO_2 (M)-V_2O_5 nanobeam heterostructures provides a new and promising oxide catalogue for building photoconductive IR detectors.

Herein we highlighted a new photoconductive NIR detector based on core/shell nanobeam heterostructures (CSNHs) with the inner single-domain monoclinic VO_2 (M) core and outer V_2O_5 shell, which is the first example of TMOs family for photoconductive IR detectors with ultrahigh performance. The excitons generated in the narrow bandgap of monoclinic VO_2 (M) nanobeam were efficiently separated due to the presence of type ‖ heterojunction formed on the VO_2 (M)-V_2O_5 heterointerface, which achieved an ultrahigh NIR sensitivity. In the as-established CSNHs-based photoconductive NIR detector, the responsivity (R_λ) of 2873.7 A W^{-1} and specific detectivity (D^*) of 9.23×10^{12} Jones are achieved at room temperature with the 990 nm wavelength irradiation and a power density of 0.2 mW cm^{-2}, recording the best IR performance compared with those reported IR detectors based on the heavy-metal-free material systems of s-SWCNTs, semiconducting graphene nanoribbons, silicon, In_2Te_3, MoS_2, and so forth (**Table 1**).

2. Results and Discussion

2.1. Fabrication of Core–Shell Nanobeam Heterostructures (CSNHs) with Inner Single-Domain Monoclinic VO_2 (M) Core and Outer V_2O_5 Shell

The formation of high-quality VO_2 (M)/V_2O_5 CSNHs relied upon the controlled synthesis of the high-quality single-domain monoclinic VO_2 (M) nanobeams. The modified growth methodology, i.e. a space-confinement chemical vapor deposition (CVD) reaction, successfully realized the easy-achieving reaction conditions such as ambient pressure and lower reaction temperature to generate the ultralong nanobeams (see Experimental Section). The computational fluid dynamics (CFD) analysis theoretically illustrated our space-confinement CVD process for the formation of VO_2 (M) nanobeams. As presented in **Figure 2**b, the schematic diagram of gas carrier flow field both inside and outside of the quartz boat is obtained by the simultaneous of continuity equation and Navier-Stokes

Table 1. Comparison of the key parameters for the present monoclinic VO_2 (M)/V_2O_5 core/shell nanobeam heterostructures and other characteristic semiconducting nanostructures-based photoconductive IR detectors.

Materials Selection		Response time	Detectivity [Jones]	Responsivity	Power density	Refs.
Heavy-metal-including materials	HgTe quantum dots	—	3×10^{10}	4.4 A W^{-1}	pW	[7]
	HgCdTe	—	4×10^{8}		0.58 mW cm^{-2}	[5]
	PbS quantum dots	20 ms		10 A W^{-1}	815 nW cm^{-2}	[20]
	PbS quantum dots	—	1.8×10^{13}	2700 A W^{-1}	80 pW	[8b]
	Graphene and PbS quantum dots	1.7s/0.26s	—	10^{7} A W^{-1}	30 pW	[13b]
	Hybrid graphene-PbS quantum dot	—	7×10^{13}	10^{8} A W^{-1}	50 fW	[13c]
Heavy-metal-free materials	s-SWCNTs/P3HT	1 ms	2.3×10^{8}	2.2 mA W^{-1}	35 mW cm^{-2}	[11]
	Graphene	—	—	6.1 mA W^{-1}	—	[21]
	Graphene nanoribbons	87s/25s	—	1 A W^{-1}	80 mW cm^{-2}	[12]
	Single layer MoS_2	—	10^{7}	0.09 mA W^{-1}	50 mW cm^{-2}	[9]
	In_2Te_3 nanowire	—	—	0.3 A W^{-1}	47.8 mW cm^{-2}	[10]
	Silicon nanowire	—	—	100 A W^{-1}	—	[22]
	VO_2 (M)/V_2O_5 core/shell nanobeam heterostructures	230/55 ms	9.23×10^{12}	2873.7 A W^{-1}	0.2 mW cm^{-2}	Present work

equation. The simulation results clearly show the presence of a recirculation zone inside the quartz boat, leading to a backward flow at the bottom. Under elevated temperature, the VO_2 (B) precursor evaporates to transform the gas phase and recirculate inside the quartz boat with the driven force of the gas flow, thus making full use of the VO_2 (B) to produce VO_2 (M) nanobeams undergoing the phase transformation from the VO_2 (B) precursor to VO_2 (M) nanobeams, with the driving force of more thermal dynamically stability for monoclinic VO_2 (M).[16b] After the reaction, the monoclinic VO_2 (M) nanobeams with high density were obtained on both sides of the two substrates at each end of the quartz boat, which assumed the length from tens to more than one hundred micrometers and width of about 500 nanometers (Figure S1–S3, Supporting Information). The single-domain monoclinic phase VO_2 (M) nanobeam at room temperature was confirmed by the evolution of phase domain structures with elevated temperature, which was observed by the optical microscopy on a typical nanobeam. Figure 2c depicts representative optical images of a typical VO_2 nanobeam grown on the SiO_2/Si substrate under heating. Notably, at room temperature, the nanobeams exhibit a pure insulating phase with bright reflection. As temperature increased to about 341 K, the multiple M and I domains appear periodically along the nanobeam axis due to the external strain induced by the elastic mismatch with

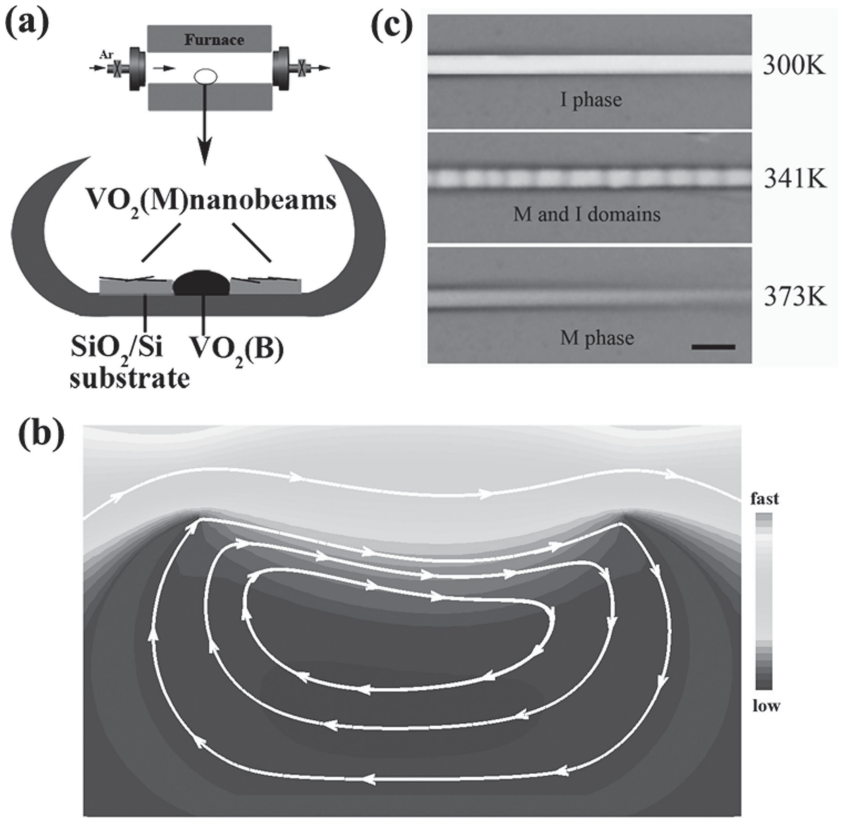

Figure 2. Space-confined CVD synthetic procedure of monoclinic VO_2 (M) nanobeam. a) The schematic diagram of the VO_2 nanobeam growth reactor for space-confined CVD process. b) The flow field simulation in the quartz boat by Computational Fluid Dynamics (CFD). c) The domain evolution of one VO_2 (M) nanobeam grown on the SiO_2/Si substrate at different temperatures of 300 K, 341 K and 373 K. Top: pure insulating (I, bright reflection) Bottom: metallic phases (M, dark reflection). Middle: coexistence of the insulating and metallic domains. Scale bars, 1 μm.

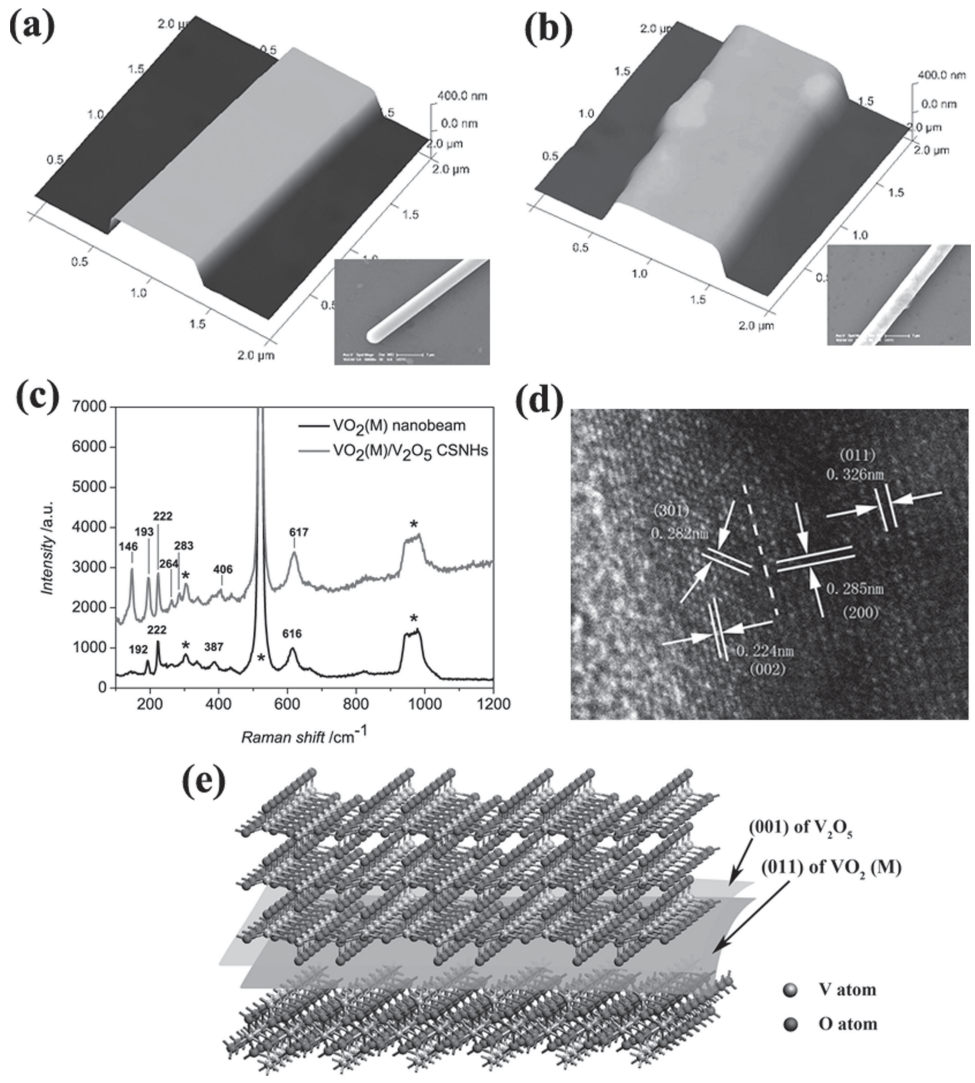

Figure 3. Microscopic characterization of VO_2 (M)/V_2O_5 CSNHs: a) AFM image of a typical monoclinic VO_2 (M) nanobeam (inset: high magnification SEM image of individual monoclinic VO_2 (M) nanobeam). b) AFM image of the VO_2 (M)/V_2O_5 CSNHs obtained by annealing of monoclinic VO_2 nanobeam in the air at 400 °C for 2 h (inset: high magnification SEM image). c) Raman spectra of monoclinic VO_2 (M) nanobeam and the VO_2 (M)/V_2O_5 CSNHs, the peaks labeled by "*" belonged to the silicon substrate. d) High resolution TEM image of the VO_2 (M)/V_2O_5 CSNHs, the distinguishing lattice fringes for the outer surface and inner core can be found suggesting the formation of VO_2 (M)/V_2O_5 core/shell structures. e) Atomic illustration of VO_2 (M)/V_2O_5 interface of CSNHs.

the substrate.[18] Finally, nanobeams converted into a single metallic phase with the dark reflection at temperature higher than the metal-insulator transition temperature (T_c). The phase domain evolution features the typical characteristics of phase changing from semiconducting monoclinic VO_2 (M) to metallic rutile VO_2 (R), verifying the presence of single-domain VO_2 (M) nanobeams around room temperature.

By heating single-domain monoclinic VO_2 (M) nanobeams at 400 °C in air, VO_2 (M)/V_2O_5 CSNHs are produced through a controlled oxidation process (see Experimental Section and Figure S4, Supporting Information). The systematic structural characterizations revealed the surface coating of orthorhombic V_2O_5 on the single-domain monoclinic VO_2 (M) with the well-defined heterogeneous interface between VO_2 (M) and V_2O_5. AFM images provided direct scenery of the surface of the CSNHs. The smooth surface of the monoclinic VO_2 (M) nanobeam as shown in **Figure 3**a became rougher after being oxidized in the air as shown in Figure 3b, exhibiting the wavy diameters of entire heated nanobeam. This phenomenon can be further verified by the high magnifying SEM images (insets in the AFM images), in which the rough surface is more obvious. The outer shell nonuniformly grew on the axial direction of the nanobeam surface, which formed the heterogeneous interfaces. Raman spectra demonstrate the coexistence of the monoclinic VO_2 (M) and the V_2O_5 phase in a single heated nanobeam. Raman spectra of the heated nanobeams show the 193 cm^{-1}, 222 cm^{-1}, and 617 cm^{-1}, which are typical peaks of pure monoclinic VO_2 (M) phase (Figure 3c); while other peaks at 146 cm^{-1}, 264 cm^{-1}, 283 cm^{-1}, and 406 cm^{-1} match well with that of the V_2O_5 phase as shown in Figure S5, Supporting Information.

The peaks labeled by star signal "*" come from the silicon substrate. The microscopic phase information of the as-obtained heterostructures provides direct evidence for the formation of heterostructural interfaces between the VO_2 (M) and V_2O_5. As illustrated in Figure 3d, the HR-TEM image is performed on the marginal edge region of the CSNHs, from which two sets of lattice fringes are distinctly observed, implying that the outer shell of the heterostructural nanobeam is crystalline V_2O_5 while the inner core is monoclinic VO_2 (M). The interplanar distance of 2.24 Å and 2.82 Å agree well with the (002) and (301) plane of V_2O_5, while the 3.26 Å and 2.85 Å spacing of the lattice fringes are indexed to the (011) and (200) plane of monoclinic VO_2 (M). The atomic illustration of VO_2 (M)/V_2O_5 heterointerface is shown in Figure 3e. All these results clearly demonstrate that the VO_2 (M)/V_2O_5 CSNHs is successfully obtained with distinguishing heterostructural interfaces through a simple epitaxial growth, which provides the necessary prerequisite for the fabrication of high performance IR detector.

2.2. Band Structure Calculations of the Oxide Heterostructures

The density functional calculations unraveled the excited photons from the monoclinic VO_2 (M), as well as the presence of band offsets between monoclinic VO_2 (M) and V_2O_5. The absolute energy levels of monoclinic VO_2 (M) and orthorhombic V_2O_5 were precisely compared using the O2s level as reference. As shown in Figure 1a,b, the calculated band structures of the monoclinic VO_2 (M) and V_2O_5 possessed the band-gap width of 0.58 eV and 2.26 eV, respectively. The smaller bandgap value of 0.58 eV is in the right response region for IR light harvesting. The energy difference of the conduction band maximum (CBM) of monoclinic VO_2 (M) and V_2O_5 is 0.28 eV, while the energy difference of the valence band minimum (VBM) is 1.97 eV, as represented in Figure 1c. Based on the calculations, the band alignment of the monoclinic VO_2 (M) and V_2O_5 heterostructures is suitable to form the type ‖ heterojunction, which effectively promotes the photogenerated excitons separation. Under IR illumination, the photogenerated electrons would transfer from the conduction band of the VO_2 (M) to that of V_2O_5 to prolong the lifetime of the photogenerated carriers shown in Figure 1d, and thus efficiently improve the IR response.

2.3. NIR Response of As-Obtained VO_2 (M)/V_2O_5 CSNHs

As expected, the as-grown monoclinic VO_2 (M)/V_2O_5 core/shell nanobeam heterostructures with well-defined type ‖ heterojunction interface achieves the intriguing IR harvesting and detection ability. As depicted in **Figure 4**b (inset), individual VO_2 (M)/V_2O_5 CSNHs was directly fabricated into the photoconductive NIR detector with two terminations contacted by a pair of

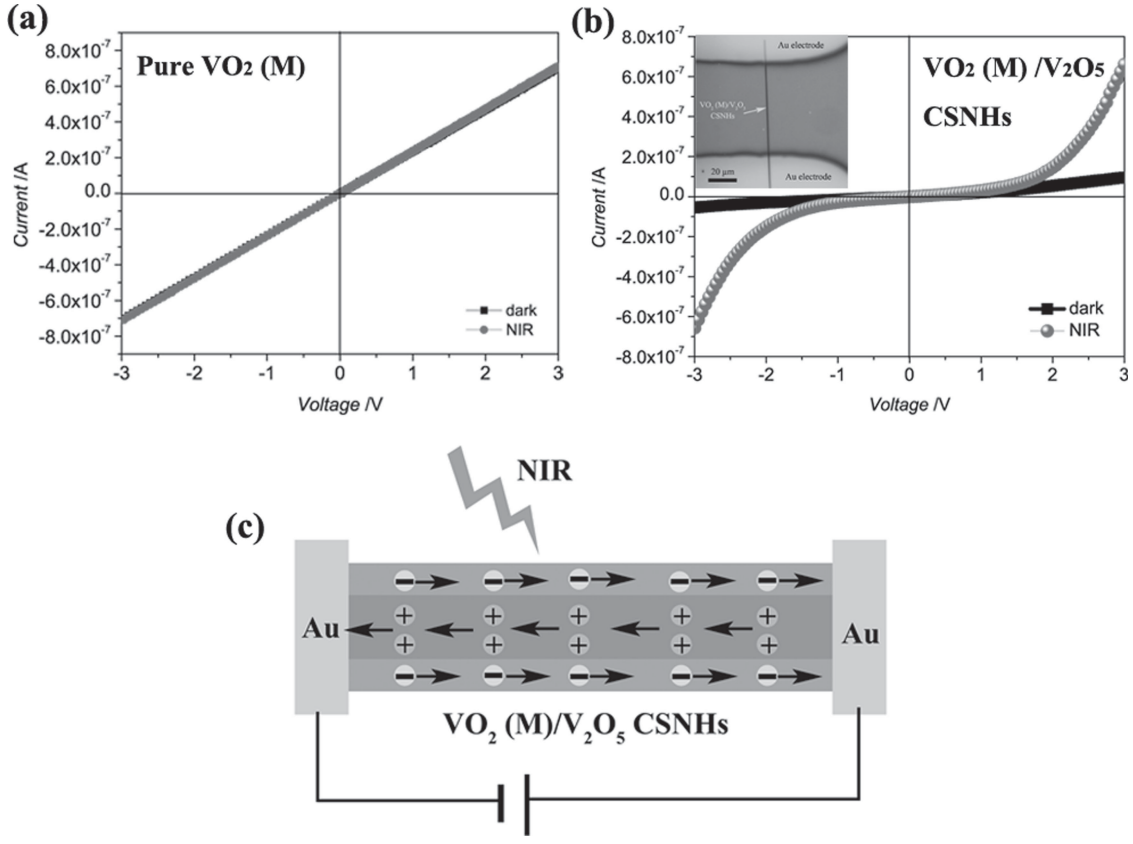

Figure 4. a) Typical *I–V* curves of a single-domain VO_2 (M) nanobeam in dark and under NIR illumination of 4 mW cm^{-2} (at 990 nm). b) Typical *I–V* curves of the VO_2 (M)/V_2O_5 CSNHs detector in dark and under NIR illumination of 4.0 mW cm^{-2} (inset: the optical image of device configuration for our photoconductive NIR detector.) c) The schematic diagram exhibiting the longitudinal section of the contacts.

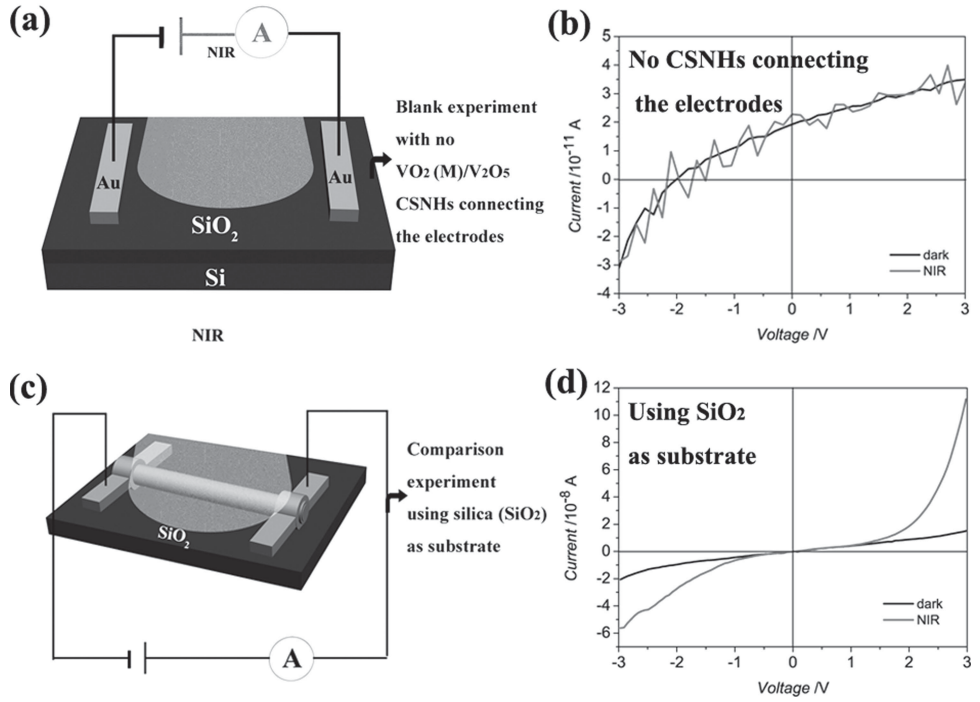

Figure 5. a) Schematics of a device with no VO_2 (M)/V_2O_5 CSNHs connecting the Au electrodes. b) *I–V* measurements of the device with no VO_2 (M)/V_2O_5 CSNHs connecting the Au electrodes in dark and under NIR illumination. c) Schematic diagram of the VO_2 (M)/V_2O_5 CSNHs photoconductive NIR detector fabricated on silica substrate. d) NIR response of the VO_2 (M)/V_2O_5 CSNHs detector fabricated on silica substrate.

Au metal electrodes which were deposited by the plasma sputtering with a copper grid shadow mask. The uncovered part of the CSNHs was exposed to the incident NIR light. The width of this CSNHs and the channel length were about 615 nm and 52 μm, respectively. *I–V* measurements were performed on this device via two probes under ambient air conditions. Figure 4b shows the typical *I–V* curves which demonstrate that the VO_2 (M)/V_2O_5 CSNHs exhibits strong NIR response at 990 nm with a power density of 4.0 mW cm^{-2} at room temperature. The *I–V* curves are extraordinary nonlinear and deviate from the linear area under larger voltage. This can be clearly confirmed from the calculated ratio of photocurrent response ΔI over dark current I_{dark} ($\Delta I/I_{dark}$). Accordingly, the $\Delta I/I_{dark}$ ratio turns out to be 1.70 under a bias of 2.0 V, and increases up to 5.90 at the 3.0 V bias. The larger NIR response is attributed to the fact that higher applied external voltage promotes the dissociation speeds of excitons at the interface of the VO_2 (M)/V_2O_5 core/shell heterostructures. As shown in Figure 4c, the photogenerated electrons transfer from the conduction band (CB) of the core VO_2 (M) to that of shell V_2O_5 under NIR illumination, leading to a high concentration of electrons in the CB of V_2O_5, while the holes are transported through the inner VO_2 (M). High voltage drives the photogenerated electrons to the external circuit effectively before they recombine with holes. And thus it results in the large photoconductivity enhancement.

As for comparison, we also investigated the NIR response behavior of pure VO_2 (M) nanobeam, a pair of Au electrodes were deposited on two terminations of an individual VO_2 (M) nanobeam by the plasma sputtering. *I–V* measurements were performed on this device by a two-probe method under ambient air conditions. As shown in Figure 4a, the approximately symmetric and linear *I–V* curves indicated the ohmic contact of the VO_2 (M) nanobeam for Au electrodes. The photocurrent under illumination of 990 nm light exhibited no apparent changes compared with that in the dark condition. This result suggested that pure VO_2 (M) nanobeam exhibited no obvious NIR response, which was attributed to the inefficient separation of the photogenerated electron-hole pairs as that in the VO_2(M)/V_2O_5 CSNHs.

To rule out the effect of the blank SiO_2/Si substrate, comparison experiments have also been conducted in the blank substrate as seen in **Figure 5**a. In this case, we sputtered the gold electrodes keeping other experimental conditions constant, and then all the measured signals could only be produced from the substrate effects. As shown in Figure 5b, there were no obvious signal changes under the external NIR light irradiation when compared with that under the black condition. In dark condition, the *I–V* curves revealed a broken circuit behavior with an ultralow current value of $\approx 10^{-11}$ A, which indicated the huge electrical resistance exceeded the measuring range of the test system; Even under the external irridiation of NIR light, the broken circuit still remains for the pure blank SiO_2/Si substrate. Our experimental fact verified that the substrate effects did not contribute the dominant NIR response.

Moreover, we found that the ultrahigh NIR response could also be found in the other relevant substrates, such as the pure silica (SiO_2) substrate. The pure silica (SiO_2) was used as the substrate for testing the NIR response of VO_2 (M)/V_2O_5 CSNHs. As depicted in Figure 5c, the VO_2 (M)/V_2O_5 CSNHs NIR detectors were also fabricated on the silica substrate by the

same experimental procedures on SiO_2/Si substrate. It can be seen in Figure 5d that with the use of silica as substrate, the VO_2 (M)/V_2O_5 CSNHs still exhibit strong NIR response, similar to that on the SiO_2/Si substrate. That is to say, our SiO_2/Si substrate could be available for the utilization of substrate for NIR test as that in the pure silica (SiO_2) substrate. All the comparison experiments verified that the effects of the substrates to the NIR could be ruled out, and the ultrahigh NIR response of our NIR detectors was indeed originated from the VO_2 (M)/V_2O_5 CSNHs.

To further investigate the NIR response of our VO_2 (M)/V_2O_5 CSNHs photoconductive NIR detector, *I–V* measurements under different irradiation power density have been performed and the ultrahigh response of our NIR detector can be reflected by the calculated results of responsivity (R_λ) and specific detectivity (D*). As shown in **Figure 6**a, the *I–V* curves are highly nonlinear and bend much more at larger voltage. The photocurrent increases with the increase of the NIR irradiation power, which is attributed to the increasing density of photogenerated electrons induced by the increasing light power density. To clearly observe the changing trend of the photocurrent with the irradiation power, the power density dependence of the photocurrent at a bia of 3.0 V is shown in Figure 6b. With the increase of applied NIR light power, photocurrent increases gradually and finally approaches to saturate when power density reaches to 4.0 mW cm^{-2}, at which photoinduced carrier separation reached the maximum value. Responsivity (R_λ) is the photocurrent generated per unit power of incident light on the effective area of a photoconductor, which can be defined as $R_\lambda = I_{ph}/(PS)$, where I_{ph} is the difference between the photoexcited current and the dark current, P is the incident light power density, S is the effective irradiated area on the individual VO_2 (M)/V_2O_5 CSNHs. Specific detectivity (D^*) is a measurement of detector sensitivity, in which we suppose that the shot noise from dark current is the major noise which is defined as $D^* = R_\lambda S^{1/2}/(2eI_d)^{1/2}$ where R_λ is the responsivity, S is the effective irradiated area on the individual heterostructure, e is the electronic charge, I_d is the dark current. Figure 6c,d show the calculated values of R_λ and D^* at different light power density. It can be seen that the values of R_λ and D^* decrease quickly when the light power density increases. At room temperature, with the power density varying from 0.2 to 4.0 mW cm^{-2}, the R_λ and D^* change from 2873.7 to 442.0 A W^{-1} and 9.23×10^{12} to 1.42×10^{12} Jones, respectively. The obtained R_λ of 2873.7 A W^{-1} and D^* of 9.23×10^{12} Jones are the best performance compared with those reported IR detectors based on the traditional heavy-metal-free material systems of s-SWCNTs ($R_\lambda \approx 2.2$ mA W^{-1}, $D^* \approx 2.3 \times 10^8$ Jones),[11] semiconducting graphene nanoribbons ($R_\lambda \approx 1.0$ A W^{-1}),[12] MoS_2 ($R_\lambda \approx 0.09$ mA W^{-1}, $D^* \approx 10^7$ Jones),[9] In_2Te_3 nanowire ($R_\lambda \approx 0.3$ A W^{-1})[10] or silicon ($R_\lambda \approx 300$ A W^{-1}, $D^* \approx 10^{13}$ Jones),[19] and even superior/comparable to the reported ones based on traditional heavy-metal-including materials of the HgTe QDs (4.4 A W^{-1}, $D^* \approx 3 \times 10^{10}$ Jones),[7] or the solution processed PbS quantum dots (QDs) ($R_\lambda \approx 2700$ A W^{-1}, $D^* \approx 1.8 \times 10^{13}$ Jones).[8b] The key parameters are compared with other photoconductive existing IR detectors as shown in Table 1.

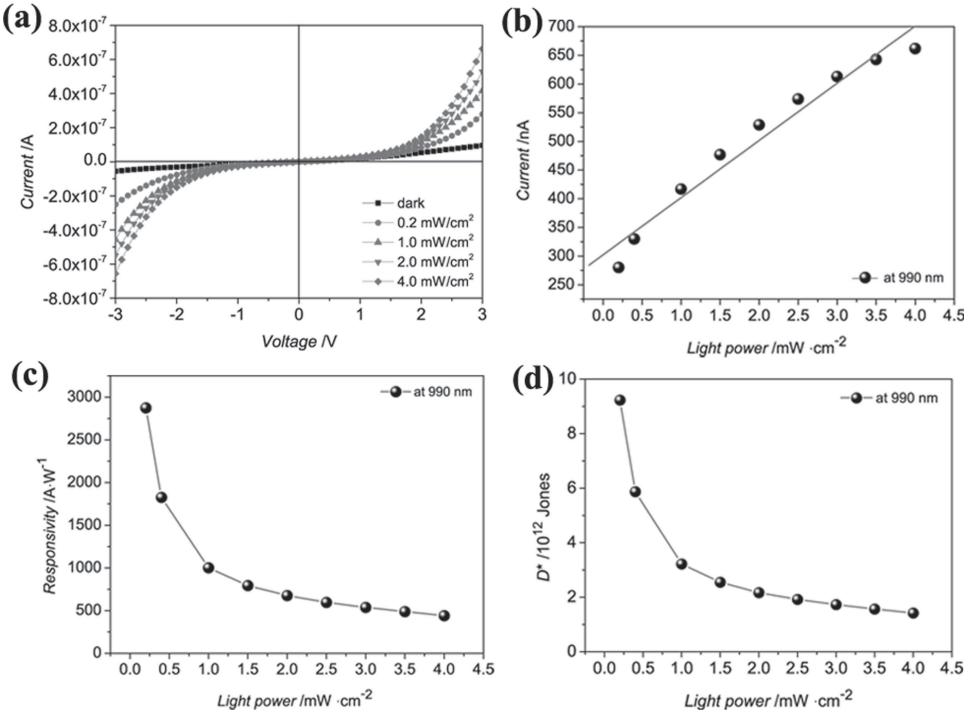

Figure 6. Photoresponse measurements of our photoconductive NIR detector at room temperature. a) Typical *I–V* curves of the VO_2 (M)/V_2O_5 CSNHs detector in dark and under NIR illumination with the power of 0.2, 1.0, 2.0, and 4.0 mW cm^{-1}. b) Curve of light power density-dependent photocurrent at a voltage of 3 V. c) Curve of light power density-dependent responsivity at a voltage of 3 V. d) Curve of light power density-dependent specific detectivity at a voltage of 3 V.

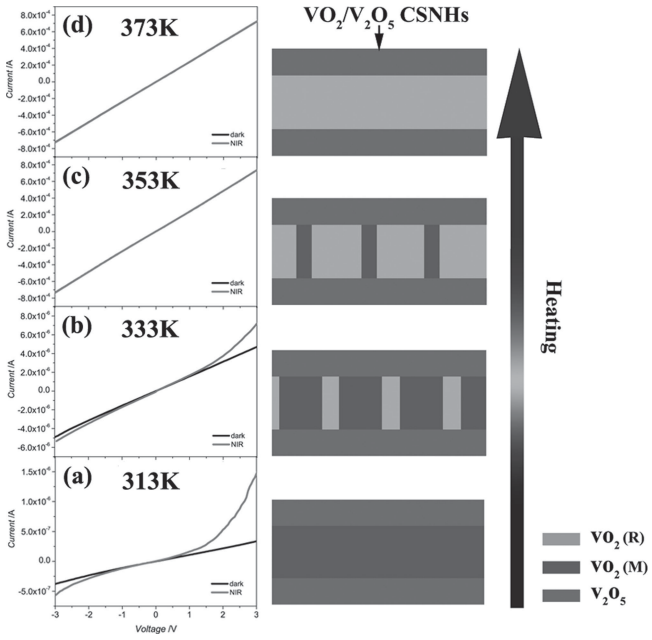

Figure 7. Infrared responses of the VO_2 (M)/V_2O_5 core/shell nanobeam heterostructures at different working temperature and the schematic diagram of the metal-insulator transition occuring in the inner VO_2 core with increasing temperature. a,b) NIR response below the metal-insulator transition temperature. c,d) NIR response above the metal-insulator transition temperature.

band, leading to ultrahigh performance of IR response. The experimental results at different working temperature verified the vital role of semiconducting monoclinic VO_2 with small band gap width that can be effectively excited under the NIR photons irradiation, ensuring the ultrahigh performance of NIR response in our case.

The VO_2 (M)/V_2O_5 CSNHs photoconductive NIR detectors also offer a good repeatability, fast response time and excellent stability. The schematic diagram of the VO_2 (M)/V_2O_5 CSNHs photoconductive NIR detector is depicted in **Figure 8**a. As shown in Figure 8b, the photoconductive NIR detector exhibits a very reversible switching measured by periodically turning on and off the 990 nm laser at a voltage of 3 V. Under NIR illumination, the photocurrent increases to a stable value and drops to the initial value rapidly when the light is turned off. Furthermore, an enlarged portion of one rising and delaying process has been shown in Figure 8c which suggests a fast response time. The photocurrent of the detector rises less than 50 ms and delays to its dark-state value within 230 ms. Such fast response time is attributed to the fast excitons separation efficiency due to the type ‖ heterojunction. On the other hand, the one dimensional nanostructure with high surface-to-volume ratio enhances the rate of photogenerated charges. It should be mentioned that the stability is a crucial factor of detectors in practical applications. Figure 8d depicts the variations in the photocurrent of our photoconductive NIR detector illuminated continuously with the laser at a bias of 3 V. No obvious degradation is observed within 2000 s, and

In order to further investigate the NIR response of the detectors at different working temperature, the typical *I*–*V* curves in dark and under NIR illumination at different working temperatures were studied. At a relative lower temperature of 313 K as shown in **Figure 7**a, the VO_2 (M)/V_2O_5 core/shell nanobeam heterostructures detector exhibits high response to the NIR. Such NIR response phenomena keeps up to the temperature of 333 K (Figure 7b), approaching to the MIT temperature (341 K). However, the gradual decrease of response can be clearly shown as elevation of working temperature. When the working temperature is over 340 K as shown in Figure 7c,d, the detector based on the VO_2 (M)/V_2O_5 core/shell nanobeam heterostructures shows no response to the NIR. At temperature > T_c, the core monoclinic VO_2 (M) was transformed into the metallic rutile VO_2 (R) and thus metallic rutile VO_2 (R) with zero bandgap could not absorb NIR photons anymore, unlike that in the low-temperature monoclinic phase. In effect, semiconducting monoclinic VO_2 (M) with small band-gap width effectively facilitated the adsorption of NIR photons which then excited the electrons from valence band to conduction

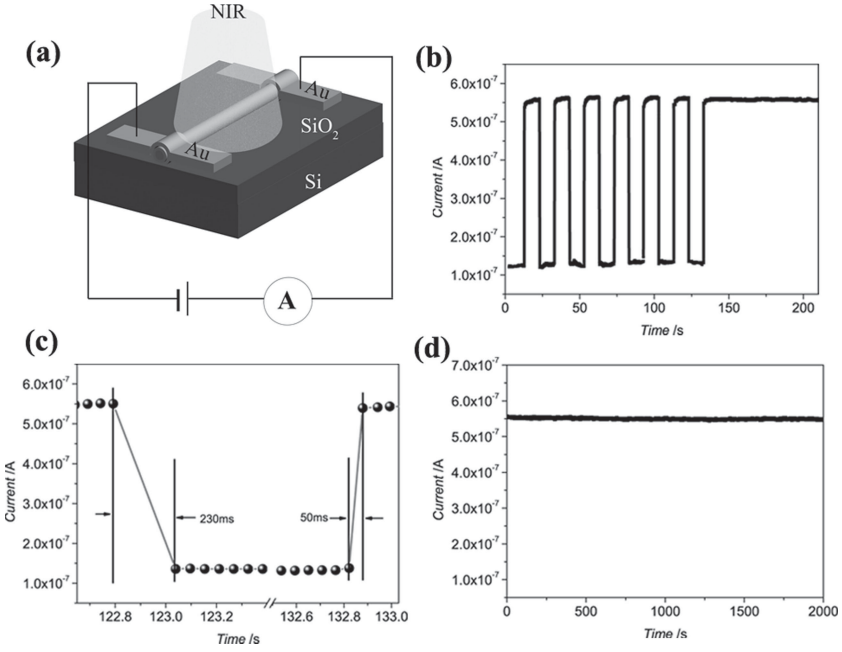

Figure 8. The repeatability, fast response time and excellent stability of our photoconductive NIR detector at room temperature. a) Schematic diagram of the VO_2 (M)/V_2O_5 CSNHs photoconductive NIR detector. b) Time-dependent photocurrent of the photoconductive NIR detector with the laser on and off at a voltage of 3 V (power density: 2.0 mW cm^{-2}, wavelength (at 990 nm). c) Enlarged portions of one rise and delay process. d) A photocurrent-time plot with a voltage of 3 V and 2.0 mW cm^{-2} power density illumination (at 990 nm).

the photocurrent fluctuation (defined as $\Delta I/I_{initial}$) is less than 1.1% which suggests the excellent photocurrent stability. Our detector remained high performance with no obvious degradation after several months, which demonstrated a good stability in the atmosphere.

3. Conclusions

In summary, we demonstrated a novel photoconductive near-infrared (NIR) detector based on new oxide catalogue of photoactive materials. Oxide-catalogue photoconductive NIR detector was built by core/shell nanobeam heterostructures (CSNHs) with inner single-domain monoclinic VO_2 (M) core and outer V_2O_5 shell, which is the first example of TMOs family for photoconductive IR detectors with ultrahigh performance. Our established photoconductive NIR detector successfully realized an ultrahigh IR detection performance under relative higher temperature, especially for room temperature condition. At room temperature, the TMO-based photoconductive NIR detector achieved ultrahigh responsivity (R_λ) of 2873.7 A W^{-1} and specific detectivity (D^*) of 9.23×10^{12} Jones at the 990 nm wavelength irradiation with a power density of 0.2 mW cm^{-2}, tracking the best performance among those reported IR detectors based on the traditional heavy-metal-free materials, and even superior/comparable to the reported ones based on heavy-metal-including materials (Table 1). Such high performance has been attributed to the fast and efficient photogenerated excitons dissociation at the oxide heterointerface with the type ‖ band alignment. Our findings pave a new way to design oxide heterostructures for intriguing applications in optoelectronic and energy harvesting nanodevices.

4. Experimental Section

Synthesis of High-Quality Single-Domain Monoclinic VO_2 (M) Nanobeams: In a typical procedure, VO_2 (B) (20 mg) fine polished powder was placed at the center of a homemade quartz boat. Two clean Si substrates covered with a 200 nm thick thermal oxide layer were laid closely to the VO_2 (B) powder, as shown in Figure 2a. Then the boat was placed at the center of a horizontal tube furnace. The furnace was initially flushed for 30 min by following high purity Ar carrier gas with a flow rate of 410 sccm (standard centimeter-cubic per minute) under ambient pressure, then elevated to the evaporation temperature of 700 °C within 70 min and maintained at a constant 700 °C for 120 min for nanobeams growth with constant Ar flow. Finally, the samples were allowed to cool to room temperature within 180 min.

Synthesis of core/shell nanobeam heterostructures (CSNHs) with inner single-domain monoclinic VO_2 (M) core and outer V_2O_5 shell: In our case, the VO_2 (M)/V_2O_5 core/shell nanobeam heterostructures was obtained by controlled oxidation of the monoclinic VO_2 (M) nanobeams in air at 400 °C. By tuning the different annealing time for 1 h, 2 h, 4 h, and 6 h, it was found that the samples annealed for 2 h yield the highest NIR response, which were chosen to fabricate into the photoconductive IR detectors in present work.

The Flow Field Simulation in the Quartz Boat by Computational Fluid Dynamics: A computational fluid dynamics (CFD) analysis is performed to obtain the structure of the gas flow. Since the flow rate is low, the gas is assumed to be incompressible or the density ρ is constant. Then the flow is governed by the continuity equation and the Navier-Stokes equation

$$\nabla \cdot u = 0,$$

$$\frac{\partial u}{\partial t} + (u \cdot \nabla)u = -\frac{1}{\rho}\nabla p + \frac{\mu}{\rho}\nabla^2 u,$$

where u is the velocity, p is the pressure, and μ is the viscosity. For simplicity, the equations are solved in a two-dimensional rectangular domain with a length 200 mm and the hight H = 39 mm. The quartz boat is 30 mm long and 14 mm high, and is located in the middle of the domain. The center line velocity of the inflow U is specified so that the Reynolds number $\mathrm{Re} = \rho U H/\mu = 10$, comparable with the experimental conditions. A standard finite-element method is employed to solve the governing equations and eventually a steady flow is obtained. The figure clearly shows the presence of a recirculation zone inside the quartz boat, leading to a backward flow at the bottom.

Characterization: Raman spectra were recorded with a LABRAM-HR Confocal Laser Micro Raman Spectrometer 750 K. The field emission scanning electron microscopy (FE-SEM) images were obtained on a JEOL JSM-6700F SEM. High-resolution TEM (HR-TEM) images were taken on a JEOL-2010 microscope at an accelerating voltage of 200 kV. The optical images were obtained on Olympus BX51M. Tapping-mode atomic force microscopy (AFM) images were taken on a DI Innova Multimode SPM platform. The electrical and photoelectric performance were measured by the Germany ZAHNER Photoelectrochemical Workstations and Keithley 4200-SCS Semiconductor characterization system.

Supporting Information

Supporting Information is available from the Wiley Online Library or from the author.

Acknowledgements

The authors thank Dr. Wen Fan at USTC and Dr. Jinbo Cao at GE for valuable advice. This work was financially supported by the National Basic Research Program of China (No. 2009CB939901), National Natural Science Foundation of China (No. 21222101, 11074229, 11132009, 11079004, 90922016, J1030412), Chinese Academy of Science (XDB01020300), and the Fundamental Research Funds for the Central Universities (No. WK2340000035 and WK2310000024). Zhenpeng at NKU thanks NSFC funding support (No. 21203099).

Received: August 24, 2013
Revised: October 2, 2013
Published online: November 18, 2013

[1] a) E. H. Sargent, *Nat. Photonics* **2009**, *3*, 325; b) M. M. Lee, J. Teuscher, T. Miyasaka, T. N. Murakami, H. J. Snaith, *Science* **2012**, *338*, 643.

[2] a) T. Rauch, M. Boberl, S. F. Tedde, J. Furst, M. V. Kovalenko, G. Hesser, U. Lemmer, W. Heiss, O. Hayden, *Nat. Photonics* **2009**, *3*, 332; b) J. S. Dam, P. Tidemand-Lichtenberg, C. Pedersen, *Nat. Photonics* **2012**, *6*, 788.

[3] S. A. McDonald, G. Konstantatos, S. Zhang, P. W. Cyr, E. J. D. Klem, L. Levina, E. H. Sargent, *Nat. Mater.* **2005**, *4*, 138.

[4] R. Lu, Z. Li, G. Xu, J. Z. Wu, *Appl. Phys. Lett.* **2009**, *94*, 163110.

[5] J. Wang, X. Chen, W. Hu, L. Wang, W. Lu, F. Xu, J. Zhao, Y. Shi, R. Ji, *Appl. Phys. Lett.* **2011**, *99*, 113508.

[6] A. Rogalski, J. Antoszewski, L. Faraone, *J. Appl. Phys.* **2009**, *105*, 091101.

[7] M. Böberl, M. V. Kovalenko, S. Gamerith, E. J. W. List, W. Heiss, *Adv. Mater.* **2007**, *19*, 3574.

[8] a) J. P. Clifford, G. Konstantatos, K. W. Johnston, S. Hoogland, L. Levina, E. H. Sargent, *Nat. Nanotechnol.* **2009**, *4*, 40; b) G. Konstantatos, I. Howard, A. Fischer, S. Hoogland, J. Clifford, E. Klem, L. Levina, E. H. Sargent, *Nature* **2006**, *442*, 180.
[9] W. Choi, M. Y. Cho, A. Konar, J. H. Lee, G.-B. Cha, S. C. Hong, S. Kim, J. Kim, D. Jena, J. Joo, S. Kim, *Adv. Mater.* **2012**, *24*, 5832.
[10] Z. Wang, M. Safdar, C. Jiang, J. He, *Nano Lett.* **2012**, *12*, 4715.
[11] R. Lu, C. Christianson, A. Kirkeminde, S. Ren, J. Wu, *Nano Lett.* **2012**, *12*, 6244.
[12] B. Chitara, L. S. Panchakarla, S. B. Krupanidhi, C. N. R. Rao, *Adv. Mater.* **2011**, *23*, 5419.
[13] a) I. Ka, V. Le Borgne, D. Ma, M. A. El Khakani, *Adv. Mater.* **2012**, *24*, 6288; b) Z. Sun, Z. Liu, J. Li, G.-a. Tai, S.-P. Lau, F. Yan, *Adv. Mater.* **2012**, *24*, 5878; c) G. Konstantatos, M. Badioli, L. Gaudreau, J. Osmond, M. Bernechea, F. P. G. de Arquer, F. Gatti, F. H. L. Koppens, *Nat. Nanotechnol.* **2012**, *7*, 363.
[14] A. Vardi, G. Bahir, F. Guillot, C. Bougerol, E. Monroy, S. E. Schacham, M. Tchernycheva, F. H. Julien, *Appl. Phys. Lett.* **2008**, *92*, 011112.
[15] a) J. H. Lee, J.-C. Chiang, S. S. Li, P. J. Kannam, *Appl. Phys. Lett.* **1999**, *74*, 765; b) K. T. Lai, S. K. Haywood, A. H. Mohamed, M. Missous, R. Gupta, *Appl. Phys. Lett.* **2005**, *87*, 192113.
[16] a) C. Wu, H. Wei, B. Ning, Y. Xie, *Adv. Mater.* **2010**, *22*, 1972; b) C. Wu, J. Dai, X. Zhang, J. Yang, F. Qi, C. Gao, Y. Xie, *Angew. Chem. Int. Ed.* **2010**, *122*, 138.
[17] F. Zhang, Y. Ding, Y. Zhang, X. Zhang, Z. L. Wang, *ACS Nano* **2012**, *6*, 9229.
[18] J. Cao, E. Ertekin, V. Srinivasan, W. Fan, S. Huang, H. Zheng, J. W. L. Yim, D. R. Khanal, D. F. Ogletree, J. C. Grossman, J. Wu, *Nat . Nanotechnol.* **2009**, *4*, 732.
[19] Y. Guo, G. Yu, Y. Liu, *Adv . Mater.* **2010**, *22*, 4427.
[20] S. Hinds, L. Levina, E. J. D. Klem, G. Konstantatos, V. Sukhovatkin, E. H. Sargent, *Adv. Mater.* **2008**, *20*, 4398.
[21] T. Mueller, F. Xia, P. Avouris, *Nat. Photonics* **2010**, *4*, 297.
[22] A. Zhang, H. Kim, J. Cheng, Y.-H. Lo, *Nano Lett.* **2010**, *10*, 2117.